Frontiers of Information Technology & Electronic Engineering
www.jzus.zju.edu.cn; engineering.cae.cn; www.springerlink.com
ISSN 2095-9184 (print); ISSN 2095-9230 (online)
E-mail: jzus@zju.edu.cn

An untethered cable-driven ankle exoskeleton with plantarflexion-dorsiflexion bidirectional movement assistance*

Tian-miao WANG[§1], Xuan PEI[§1], Tao-gang HOU[§1,2], Yu-bo FAN[3,5], Xuan YANG[1], Hugh M. HERR[†‡4], Xing-bang YANG[†‡4]

[1]*School of Mechanical Engineering and Automation, Beihang University, Beijing 100083, China*
[2]*Shenyuan Honors College, Beihang University, Beijing 100083, China*
[3]*School of Biological Science and Medical Engineering, Beihang University, Beijing 100083, China*
[4]*MIT Media Lab, Massachusetts Institute of Technology, Cambridge, MA 02139-4307, USA*
[5]*Beijing Advanced Innovation Center for Biomedical Engineering, Beihang University, Beijing 100083, China*
[†]E-mail: hherr@media.mit.edu; xingbang@mit.edu

Received Aug. 30, 2019; Revision accepted Apr. 21, 2020; Crosschecked Apr. 30, 2020

Abstract: Lower-limb assisted exoskeletons are widely researched for movement assistance or rehabilitation training. Due to advantages of compliance with human body and lightweight, some cable-driven prototypes have been developed, but most of these can assist only unidirectional movement. In this paper we present an untethered cable-driven ankle exoskeleton that can achieve plantarflexion-dorsiflexion bidirectional motion bilaterally using a pair of single motors. The main weights of the exoskeleton, i.e., the motors, power supplement units, and control units, were placed close to the proximity of the human body, i.e., the waist, to reduce the redundant rotation inertia which would apply on the wearer's leg. A cable force transmission system based on gear-pulley assemblies was designed to transfer the power from the motor to the end-effector effectively. A cable self-tension device on the power output unit was designed to tension the cable during walking. The gait detection system based on a foot pressure sensor and an inertial measurement unit (IMU) could identify the gait cycle and gait states efficiently. To validate the power output performance of the exoskeleton, a torque tracking experiment was conducted. When the subject was wearing the exoskeleton with power on, the muscle activity of the soleus was reduced by 5.2% compared to the state without wearing the exoskeleton. This preliminarily verifies the positive assistance effect of our exoskeleton. The study in this paper demonstrates the promising application of a lightweight cable-driven exoskeleton on human motion augmentation or rehabilitation.

Key words: Ankle exoskeleton; Plantarflexion-dorsiflexion bidirectional assistance; Biological gait torque; Cable-driven; Gait detection
https://doi.org/10.1631/FITEE.1900455 **CLC number:** TP242.6

1 Introduction

There is now a lot of research on the lower-limb assisted exoskeleton, something which can be used to assist exercise or in rehabilitation training (Dong et al., 2018; He et al., 2019). These exoskeletons help the wearers realize normal movement or augment the movement, such as walking (Miller et al., 2016), running (Cherry et al., 2016), and going up and down stairs (Jatsun et al., 2017).

‡ Corresponding authors
§ The three authors contributed equally to this work
* Project supported by the National Natural Science Foundation of China (No. 61703023), Beijing Municipal Natural Science Foundation, China (No. 3184054), China Scholarship Council (No. 201706025021), and National Undergraduate Training Programs for Innovation and Entrepreneurship (No. 201910006118)
ORCID: Hugh M. HERR, https://orcid.org/0000-0003-3169-1011; Xing-bang YANG, https://orcid.org/0000-0003-0387-6043

Most traditional untethered lower-limb exoskeletons are typically driven by electrical motors or hydraulic actuators, which are assembled at each joint of the human body. For instance, Zoss et al. (2005) designed a prototype using four linear hydraulic actuators to drive hip (flexion/extension and abduction/adduction), knee (flexion), and ankle (plantarflexion/dorsiflexion) per leg. Farris et al. (2011) made an exoskeleton which can help the spinal cord-injured (SCI) individuals by providing assistance torques at both hip and knee joints and is driven by electrical motors. In addition, Sankai (2010) proposed the concept of Cybernics that combines human, machine, and information systems. This system significantly promotes the human–machine coordination performance of the exoskeleton. However, these joint-actuator based designs, whose actuator, power supply unit, and control unit are directly connected with the wearer's legs, often make the device too bulky, heavy, and inconvenient to wear (Rupal et al., 2016). At the same time the rotational inertia applied to the wearer is large because of the extra mass. This creates a burden for the users and additional physical energy consumption (Browning et al., 2007). To reduce the extra weight, two methods have been proposed for exoskeletons, i.e., to reduce mass using a passive device and to allocate the main mass remotely and off-board using tethered techniques. Passive exoskeletons (Collins et al., 2015; Kim et al., 2015; Diller et al., 2016) are lightweight because they need only springs and clutches to store and release power to assist human joint movement. For instance, Collins et al. (2015) designed an ankle exoskeleton equipped with a tension spring and a ratchet. The spring was constantly stretched and engaged by the ratchet to store energy when the foot heel struck the ground. Then, when the foot pushed off, the ratchet disengaged the spring to assist the ankle motion. However, the prototype cannot provide enough power for the wearer because of the lack of outer energy supply. Therefore, another design concept called tethered exoskeleton has been proposed, whose energy supply, controller, motor, and other heavy parts are off-board, and the wearer needs only to wear the lightweight end-effector (Witte et al., 2015; Galle et al., 2017; Kuan et al., 2018). However, people wearing this tethered exoskeleton can only move around the energy supply device, and the range of movement is extremely limited.

To combine the advantages of being lightweight, having high power output, and portability, and to reduce the redundant rotational inertia applied to the wearer's leg, some researchers have proposed to place the exoskeleton's heavy parts, i.e., motors, power supplement units, and control units, on the proximity (waist) of the human body. To achieve long-distance power transmission, related studies used a pneumatic tube or cable to transmit power between the actuator and the end-effector of the exoskeleton. Park et al. (2014) made an untethered ankle-foot exoskeleton powered with pneumatic artificial muscles. A soft exosuit designed by Wehner et al. (2013) can provide gait assistance through pneumatic actuators named "McKibben Actuators." However, compared to pneumatic actuation, an electric motor has the advantage of more precise control (Hou et al., 2019). This is very important for gait rehabilitation (Ruiz et al., 2006). With the good fit of a motor-based cable-driven system, the subject will feel more comfortable (Morris and Shoham, 2009). Another soft exosuit designed by Asbeck et al. (2014) is capable of powering multiple joints with Bowden cables. Kuan et al. (2018) solved disadvantages of the cable-driven device, such as inefficiency, nonlinear backlash, and cable tension variation using rolling cable transmissions (RoCT). Therefore, the cable-driven method is a potentially superior power transmission system for exoskeletons. However, most current cable-driven ankle exoskeletons achieve only plantarflexion movement. This recognizes that the normal ankle power output of an individual is concentrated mostly in the plantarflexion stage (Meijneke et al., 2014; Bai et al., 2015; Wu et al., 2019). For example, Meijneke et al. (2014) presented an ankle exoskeleton which could generate 52% of the positive plantarflexion power around the ankle of an 80-kg individual. Even so, bidirectional movement of the ankle in rehabilitation training is indispensable (Park et al., 2014), especially for patients with nerve injury, postoperative muscle atrophy, stroke, or other diseases (Stewart, 2008; Forrester et al., 2011; Lairamore et al., 2011). Some exoskeleton prototypes have been developed to realize bidirectional assistance. For instance, Awad et al. (2017) expanded the scope of the soft exosuit and used a Bowden cable to effect bidirectional assistance for stroke patients. Noda et al. (2018) designed a new

force-transmission system using cylinders and a Bowden cable for bidirectional ankle assistance. Zhang et al. (2019) preliminarily proposed a bidirectional cable-driven powered ankle–foot orthosis using two motors and discussed the idea of using just one motor to control plantarflexion and dorsiflexion motion. The above prototypes, which applied two actuators to realize bidirectional assistance, increased the weight and complexity of the system. An exoskeleton device using a single motor to achieve plantarflexion-dorsiflexion bidirectional ankle assistance is developed in this paper.

We present an untethered ankle exoskeleton that can achieve plantarflexion-dorsiflexion bidirectional motion using cable-driven transmission. The prototype is shown in Fig. 1. The system can efficiently transfer the power from the motor mounted at the waist to the end-effector through a force transmission system with gear-pulley assemblies. The gait cycle of the human is detected in real time using the foot pressure sensor and the inertial measurement unit (IMU). Combined with the force sensor to achieve force feedback control, the exoskeleton can provide real-time power matching the corresponding human biological data (ankle torque) during walking, while achieving ankle plantarflexion-dorsiflexion bidirectional movement through four cables at the heel and forefoot respectively.

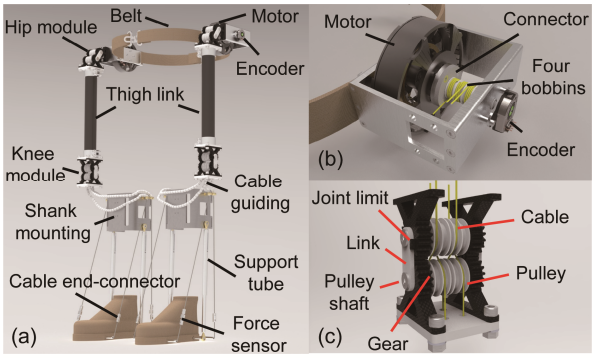

Fig. 1 Overview of our untethered cable-driven ankle exoskeleton (a), overview of the power output module (b), and a detailed diagram of the knee module of the cable transmission system (c)

In (a), the power of the motor can be transferred to the end-effector by cables and the transmission system, and the plantarflexion-dorsiflexion bidirectional motion of the ankle is achieved by clockwise or counterclockwise rotation of the motor (seen from the encoder to the motor). In (b), the motor shaft drives four bobbins to rotate, wherein the first and fourth bobbins are wound counterclockwise and connected to the forefoot, and the second and third bobbins are wound clockwise and connected to the heel. In (c), four cables wind through the pulley assembly, and a joint limit is designed to ensure safety

2 Materials and methods

2.1 Mechanical design

2.1.1 End-effector

The end-effector is the part of the exoskeleton interacting directly with the human foot as shown in Fig. 2. For the human foot during walking, the rotation and translation motion of the ankle joint in the sagittal plane is dominant (Sawicki and Khan, 2016). Therefore, the design of the end-effector is focused mainly on assisting movement of the ankle joint. It is a design principle of the end-effector that it does not interfere with movements of other planes (coronal plane, transverse plane) or other joints (knee, hip) of the body.

Based on the design requirements above, we completed the end-effector structure as shown in Fig. 2. A special shoe was made with four cables (Dyneema cable, maximum load weight of 140 kg). Fig. 2 shows only two of the cables. To balance the torque generated by the end-effector in the coronal plane, another two cables were set on the other side of

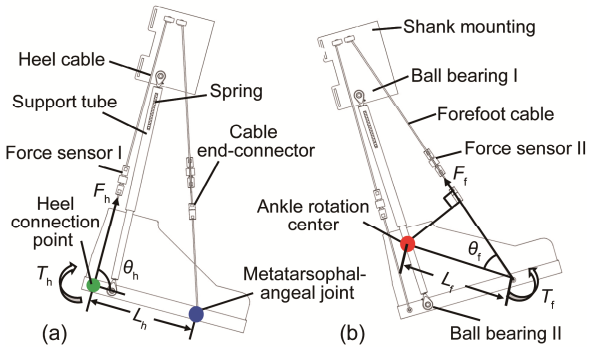

Fig. 2 Force and movement analysis of the ankle motion in the sagittal plane with the exoskeleton on: (a) plantarflexion; (b) dorsiflexion

F_h: tension force on the heel cable; L_h: length between the heel connection point and the center of the rotation; θ_h: application angle of F_h; T_h: heel moment; F_f: tension force on the forefoot cable; L_f: length between the forefoot connection point and the center of the rotation; θ_f: application angle of F_f; T_f: forefoot moment. The moment arm of T_h can be described as $L_h \cdot \sin\theta_h$ and that of T_f is $L_f \cdot \sin\theta_f$

the shoe, parallel to the two cables shown in Fig. 2. Thus, there were four cables in total acting on the end-effector. One pair was fastened at the heel of the shoe and the other pair was fixed at the forefoot of the shoe close to the metatarsophalangeal joint of the foot. To realize cable pre-tensioning, a pair of cable end-connectors was used to connect the cable segments between the shoe and the shank mounting. In addition, a pair of support tubes was designed to support shank mounting, and a spring was placed in the tube to make the tube length adjustable. In order not to restrict movement in the coronal plane or transverse plane, ball bearings were provided at both ends of the support tube.

For the plantarflexion assistance of the ankle, as shown in Fig. 2a, the cable at the heel is tensioned by the motor to provide the assistance force, and the metatarsophalangeal joint acts as the center of rotation. The tension force on the heel cable F_h can be measured by the force sensor I (ZZ210-013, Zhizhan Measurement & Control, Shanghai, China) connected in the cable, and the length between the heel connection point and the center of the rotation is L_h; thus, the heel moment T_h provided by the exoskeleton can be expressed as

$$T_h=F_hL_h\sin\theta_h, \tag{1}$$

where θ_h is the application angle of F_h, the value of which will change along with the ankle plantarflexion.

For the dorsiflexion assistance of the ankle, as shown in Fig. 2b, the forefoot cable is tensioned by the motor, and the ankle rotation center acts as the center of rotation. The tension force on the forefoot cable F_f can be measured by the force sensor II connected in the forefoot cable, and the length between the forefoot connection point and the center of the rotation is L_f. Therefore, the forefoot moment T_f can be expressed as

$$T_f=F_fL_f\sin\theta_f, \tag{2}$$

where θ_f is the application angle of F_f, the value of which will change along with the ankle dorsiflexion movement.

The forefoot cable application angle θ_f and heel cable application angle θ_h, as well as the ankle rotation angle θ_a, in a gait cycle are obtained by a video-based experiment. θ_a is defined as the angle between the line perpendicular to the calf and the line parallel to the sole, and the increase and decrease of θ_a indicate dorsiflexion and plantarflexion, respectively. In the video-based experiment, we put a marker on the shoe coaxial to the ankle rotation center, and used an action camera (Hero7 Black, GoPro Inc., California, USA) to capture the motion of the ankle when a subject walked at the speed of 3 km/h on the treadmill. Then we obtained θ_h, θ_f, and θ_a by marking and following some feature points in the motion analysis software (ProAnalyst, Xcitex Inc., Woburn, USA), as shown in Fig. 3a. The forefoot cable application angle θ_f, heel cable application angle θ_h, and ankle rotation angle θ_a versus time in a gait cycle are shown in Fig. 3b.

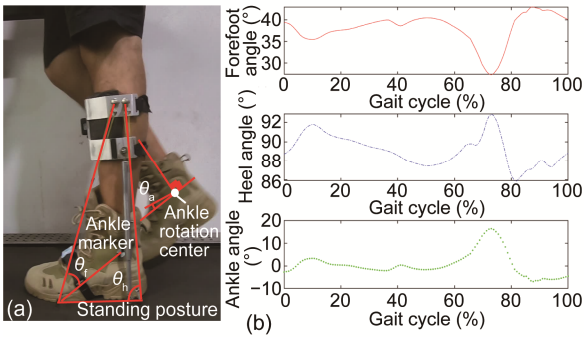

Fig. 3 Measurement of the forefoot cable angle θ_f, heel cable angle θ_h, and ankle rotation angle θ_a

(a) Definitions of angles θ_f, θ_h, and θ_a at a standing posture; (b) The ankle and cable angles change with the gait cycle. The red solid line, blue dashed line, and green dotted line represent time history of angles θ_f, θ_h, and θ_a in one gait cycle, respectively. The angles were obtained by motion analysis software ProAnalyst. References to color refer to the online version of this figure

2.1.2 Power transmission

To reduce the redundant rotation inertia applying to the wearer's leg, the motors, power supplement units, control units, etc. of the device are configured at the waist, so an effective power transmission system is very important. Kuan et al. (2018) proposed a cable transmission method, RoCT, which uses a pulley assembly to achieve zero backlash and force balance. The RoCT device can make the cable keep constant length and tensioned when the joint rotates. This ensures that the force on the cable is not disturbed by the

joint motion. The RoCT device has less power loss and backlash than the Bowden cable. Therefore, this transmission method can be applied to the power transmission of hip and knee modules in our exoskeleton, and the knee module is shown in Fig. 1c. The kinematic analysis of the transmission module is shown in Fig. 4a. Gears 1 and 2 are assembled on link O_1O_2 and meshed with each other, making the angular velocities of two gears equal in magnitude and opposite in direction. Two pulleys (pulleys 1-1, 1-2 or pulleys 2-1, 2-2) are placed concentrically with each gear on the pulley assembly, as shown in Fig. 4c. The two gears and four pulleys make up a pulley assembly.

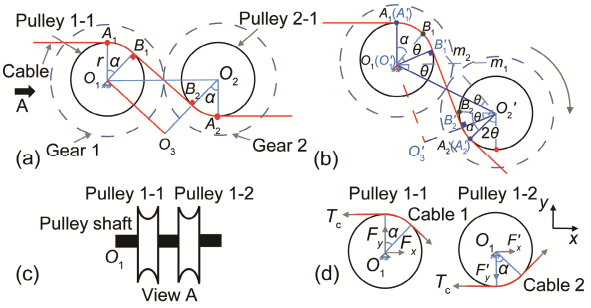

Fig. 4 A section view of the pulley assembly, composed of four pulleys (pulleys 1-1, 1-2, 2-1, 2-2) and two gears (gears 1, 2) (a), kinematic analysis after gear 2 is rotated around gear 1 with an angle θ clockwise (b), partial view from view A (c), and the force analysis of pulleys 1-1 and 1-2 (d)

The blue dashed line is the meshing line of gears. The red solid line represents the cable winding through two pulleys. When the two cables (red solid lines) which are used to drive plantarflexion or dorsiflexion wind pulleys 1-1 and 1-2 on different sides, the radial forces can be potentially reduced because F_y and F_y' are always in the opposite direction. Therefore, the tension on the cables can be transmitted to the ankle joint with a higher power ratio, avoiding the rotation of the pulley assembly due to extra force induced by the cables. References to color refer to the online version of this figure

To analyze the cable length passing through the pulley assembly, it is assumed that gear 1 is fixed and gear 2 can rotate around gear 1 as shown in Fig. 4a, and the mesh link O_1O_2 is horizontal at the beginning. The wrap angles of the cable on pulleys 1-1 and 2-1 are both α, and the radii of all the pulleys are r. Then the total length l_1 of the cable in the pulley assembly at this state can be expressed as

$$l_1 = \overset{\frown}{A_1B_1} + \overline{B_1B_2} + \overset{\frown}{B_2A_2} = 2r\alpha + \overline{B_1B_2}, \tag{3}$$

where $\overline{B_1B_2}$ is the inner common tangent between the two pulleys (pulleys 1-1 and 2-1). Then gear 2 rotates by θ clockwise around the central axis of gear 1, as shown in Fig. 4b. This results in gear 2 rotating by 2θ around its own axis. The total length l_2 of the cable in this state can be expressed as

$$l_2 = \overset{\frown}{A_1'B_1'} + \overline{B_1'B_2'} + \overset{\frown}{B_2'A_2'}. \tag{4}$$

Because the center distance O_1O_2 of the two pulleys is constant, it can be found that

$$\triangle O_1O_2O_3 \cong \triangle O_1'O_2'O_3'. \tag{5}$$

Then the following equations can be derived:

$$\overline{B_1B_2} = \overline{B_1'B_2'}, \tag{6}$$

$$\angle B_1O_1O_2 = \angle O_1O_2B_2 = \angle B_1'O_1'O_2' = \angle O_1'O_2'B_2'. \tag{7}$$

Referring to auxiliary lines O_1m_1, $O_2'm_2$ ($O_1m_1 \perp A_1O_1$, $O_2'm_2 \perp O_2'A_2$), and comparing Fig. 4a with Fig. 4b, we can obtain the following relationships:

$$\angle m_2O_2'B_2 = \angle O_1'O_2'B_2', \tag{8}$$

$$\angle B_1O_1B_1' = \angle m_1O_1'O_2' = \angle B_2O_2'B_2' = \angle m_2O_2'O_1' = \theta. \tag{9}$$

The sum of two arc lengths $\overset{\frown}{A_1'B_1'}$ and $\overset{\frown}{B_2'A_2'}$ can be expressed as

$$\begin{aligned}\overset{\frown}{A_1'B_1'} + \overset{\frown}{B_2'A_2'} &= r\angle A_1'O_1'B_1' + r\angle B_2'O_2'A_2' \\ &= r(\alpha+\theta) + r(\alpha-\theta) = 2r\alpha.\end{aligned} \tag{10}$$

According to Eqs. (3), (4), (6), and (10), the total length l_2 of the cable can be presented as

$$l_2 = \overline{B_1'B_2'} + \overset{\frown}{A_1'B_1'} + \overset{\frown}{B_2'A_2'} = \overline{B_1'B_2'} + 2r\alpha = l_1. \tag{11}$$

It can be concluded that when gear 2 rotates around gear 1, the total length of the cable between the two pulleys remains unchanged; i.e., the motion of the motor can always be approximately linearly transmitted to the end-effector. This can potentially

improve the transmission efficiency.

Force analysis of the two pulleys on the same axis (pulleys 1-1 and 1-2) was also conducted. To balance the radial force of the pulley shaft generated by the two cables used to drive plantarflexion or dorsiflexion, the two cables were wound on pulleys 1-1 and 1-2 from different sides (Figs. 4c and 4d). Thus, we can obtain the following equations:

$$\begin{cases} F_x = T_c(1-\cos\alpha), \\ F_y = T_c \sin\alpha, \end{cases} \tag{12}$$

$$\begin{cases} F_x' = T_c(1-\cos\alpha), \\ F_y' = -T_c \sin\alpha. \end{cases} \tag{13}$$

The tension forces on the two cables (red solid line in Fig. 4d) are both T_c, and the forces of pulleys 1-1 and 1-2 applying on the pulley shaft on the x axis are F_x and F_x', respectively. The force components in the y axis are F_y and F_y', respectively. According to Eqs. (12) and (13), it can be concluded that the resultant force exerting on the pulley shaft in the radial direction is potentially reduced because F_y and F_y' are always in the opposite direction.

2.1.3 Power output module

The cables used to transmit power to the exoskeleton are driven by bobbins connected to the motor axis. The forefoot cable and heel cable work with different stroke lengths at the end-effector, while the motor axis angular velocities are the same. Therefore, a tensioning device is needed to compensate for the cable length difference.

A theoretical analysis was conducted to acquire the length difference between the heel cable and the forefoot cable of our exoskeleton when a human being was walking with a normal gait. The diagram presenting the relative relation between the end-effector and the lower limb is shown in Fig. 5a. $\overline{OA}$ denotes the length from the cable go-through hole in the shank mounting to the ankle rotation center, $\overline{AB}$ is the length from the ankle rotation center to the heel, $\overline{AC}$ represents the length from the ankle rotation center to the metatarsophalangeal joint, β_0 is the angle between $\overline{OA}$ and $\overline{AB}$ at the standing position, and the angle between $\overline{OA}$ and $\overline{AC}$ is α_0. L_{hc} and L_{fc} are

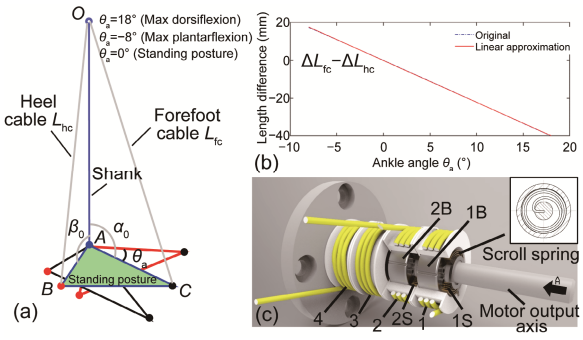

Fig. 5 A diagram showing the foot under three states (a), the length difference between the two cables calculated from the basic parameters ($\overline{OA}$ =340 mm, $\overline{AB}$ =90 mm, $\overline{AC}$ =150 mm, α_0=120°, β_0=160°) (b), and a cable length self-tensioning device diagram (c)

In (a), the red frame presents the foot in the maximum dorsiflexion position, the black frame shows the foot in the maximum plantarflexion position, and the blue frame is the foot in the standing posture. The two gray lines are the cables at the heel and the forefoot. In (b), the curve can be approximated to a linear function, which can be described as y=−2.2131x−0.0601 (r^2=0.999 98). In (c), the four cables used for power transmission are wound on bobbins 1, 2, 3, and 4. Bobbins 2 and 3 are clockwise winding (perspective from view A) to realize dorsiflexion, and bobbins 1 and 4 are counterclockwise winding to achieve plantarflexion. References to color refer to the online version of this figure

the lengths of the heel cable and forefoot cable, respectively. θ_a denotes the ankle rotation angle, as defined in Section 2.1.1, the range of which can be obtained from Fig. 3b (bottom), i.e., $\theta_a \in [-8°, 18°]$.

According to the cosine theorem, the lengths of the heel cable and forefoot cable can be respectively presented as

$$L_{hc}(\theta_a) = \sqrt{\overline{OA}^2 + \overline{AB}^2 - 2\overline{OA}\cdot\overline{AB}\cos(\beta_0+\theta_a)}, \tag{14}$$

$$L_{fc}(\theta_a) = \sqrt{\overline{OA}^2 + \overline{AC}^2 - 2\overline{OA}\cdot\overline{AC}\cos(\alpha_0-\theta_a)}. \tag{15}$$

The length difference between the two cables changing along with the rotation angle of the ankle can be expressed as

$$\begin{aligned} \Delta L(\theta_a) &= \Delta L_{fc}(\theta_a) - \Delta L_{hc}(\theta_a) \\ &= [L_{fc}(\theta_a) - L_{fc}(0)] - [L_{hc}(\theta_a) - L_{hc}(0)]. \end{aligned} \tag{16}$$

Then the function of length difference $\Delta L(\theta_a)$ (Eq. (16)) can be approximated to a linear function,

i.e., $y=-2.2131x-0.0601$ ($r^2=0.999\,98$), as shown in Fig. 5b. This length difference $\Delta L(\theta_a)$ can be used as a reference to design the tensioning device.

As shown in Fig. 5c, we constructed a cable length self-tensioning device based on the above analysis. The four cables used for power transmission are wound on bobbins 1, 2, 3, and 4. Bobbins 2 and 3 are clockwise wound (perspective from view A) to realize dorsiflexion, and bobbins 1 and 4 are counterclockwise wound to achieve plantarflexion. Each bobbin has a scroll spring S and a bearing B, and they can work together to tension the cable. For instance, springs 1S of bobbin 1 and 2S of bobbin 2 are mounted in the opposite direction. Once the motor output axis rotates clockwise, the scroll spring 2S is working in the loose state and fixed to the inner wall of the bobbin, which makes bobbin 2 rotate with the motor axis synchronously and roll up the cable on bobbin 2.

At the same time, the scroll spring 1S is in the tight state and the outer ring of the bearing 1B is driven by the motor output axis through the scroll spring 1S. This allows bobbin 1 to rotate asynchronously with the motor output axis to release the cable. Therefore, bobbins 1 and 2 can rotate with different angular speeds, which can compensate for the stroke length difference of the forefoot cable and heel cable. Similarly, when the motor output axis rotates counterclockwise, the scroll spring 1S will release the pulling force and come into the loose state to make bobbin 1 rotate synchronously, while the scroll spring 2S is in the tight state, which drives bobbin 2 to rotate asynchronously.

2.2 Gait cycle detection

The control strategy of the exoskeleton matches the human gait cycle. Fig. 6 shows the different states of a normal gait cycle. Taking the right leg as an example, the gait cycle starts from a heel strike, followed by foot flat, push off, toe off, mid swing, and finally back to heel strike. In addition, depending on whether the leg is off the ground, the gait cycle can be divided into two phases, i.e., stance phase (on the ground) and swing phase (off the ground). The stance phase, which starts from heel strike and ends by toe off, accounts for about 60% of the total gait cycle; the swing phase, which starts at toe off and ends with heel strike, accounts for about 40% of the total gait cycle (Taborri et al., 2016). Then, how the left and right legs work together during walking was investigated. Compared with the gait cycle of the right leg shown in Fig. 6, the gait cycle of the left leg is around 50% later than that of the right leg.

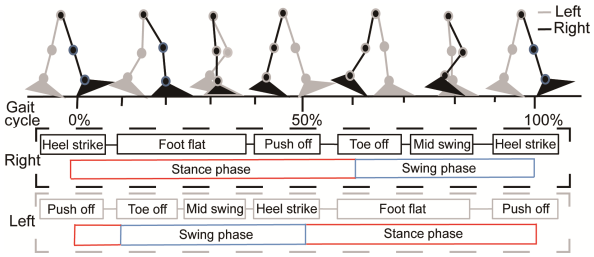

Fig. 6 State definition of a human gait cycle
The gray and black frames represent the gait cycle of the left and right legs, respectively. References to color refer to the online version of this figure

To detect the gait state, a foot pressure sensor and an IMU based gait cycle detection unit were developed. It has been reported that the plantar pressure is distributed mainly in three parts, i.e., forefoot, toe, and heel (Kyeong et al., 2019). The starting time and magnitude of the pressure profiles of the three parts are significantly different when the foot is in different states of one gait cycle. Therefore, the pressures of the three parts can be used to identify the gait state. As shown in Fig. 7a, a pair of insole-shaped foot pressure sensors (RX-ES39, Roxi Technology, Jiangsu, China) was used and put in the shoes. Once the pressure on the pressure sensor increases, the electrical resistance connected into the voltage divider circuit will be greatly reduced, thus representing the plantar pressure variation by the voltage value. Assume that the pressure state is 1 if the pressure obtained from the sensor exceeds a threshold. If the pressure is within the threshold, the pressure state is 0. Then a gait detection logic table according to the foot pressure state of the forefoot, toe, and heel is shown in Table 1. It can be concluded that the plantar pressure is zero during the swing phase, during which the gait cannot be divided by the foot pressure sensor.

However, due to squeezing, noise, or other disturbances in the shoe, using only the foot pressure sensor cannot reliably divide the gait cycle. To divide gaits more accurately and efficiently, the IMU (WT901C485, WitMotion, Shen-zhen, China), which can give three-axis acceleration, angular velocity, and

spatial angle, was also chosen as a part of the gait detector. The IMU is widely used on wearable devices since it is a lightweight, portable, safe sensor compatible with the human body (Mancini et al., 2016). The IMU was attached on the shoe of our exoskeleton, and the coordinate system was also specified as shown in Fig. 7b. The *x*-axis angle and angular velocity of the IMU were used mainly to detect the gait cycle.

Table 1 Gait detection logic table according to the foot pressure distribution

Gait	State		
	Toe	Forefoot	Heel
Heel strike	0	0	1
Foot flat	1	1	1
Push off	1	1	0
Toe off	0	0	0

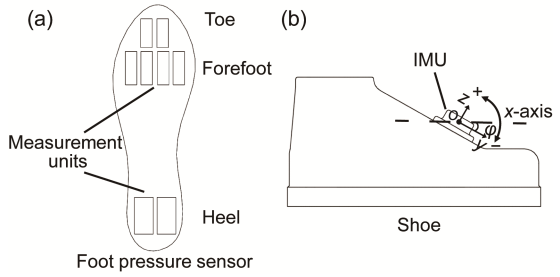

Fig. 7 Measurement units of the toe, forefoot, and heel of the foot pressure sensor (a) and placement of the IMU (b) The coordinate definition is also specified. The *yoz* plane is the sagittal plane of the human foot, and the *x* axis is defined according to the right-hand rule from the *y* axis to the *z* axis. φ is the pitch angle around the *x* axis of the IMU

2.3 Controller design

2.3.1 Controller hardware

The microprogrammed control unit (MCU, STM32F103, STMicroelectronics, Geneva, Switzerland) was chosen as the central processing unit. The left leg and right leg sensor systems are shown in Fig. 8 (red and blue frames). The signal of the force sensor was amplified by the differential amplifier chip AD620 and transmitted to the MCU by the built-in 12-bit analog-to-digital converter (ADC). The IMU communicated with the MCU by the RS485 bus (level-converted by MAX485). The heel, forefoot, and toe pressures of the foot pressure sensor were selected by the dual four-channel multiplexer CD4052 and then transmitted by the ADC to the MCU.

The motor control system is shown in Fig. 8 (green frame). The brushless DC (BLDC) motor (U12 KV90, T-Motor, Jiangxi, China) was chosen to drive the prototype. The position and velocity of the motor were measured by the incremental encoder (AMT103-V, CUI Inc., Oregon, USA). Correspondingly, an open source BLDC motor controller (v3.5 48V, ODrive, USA), which can communicate with MCU through the universal asynchronous receiver/transmitter (UART), was used to control the motor. A Li-Po battery (R-FLY 5300mah 75C, ACE, Shenzhen, China) was selected as the energy supply. Therefore, the MCU could compute the desired torque and send the command to the ODrive motor controller at a frequency of 120 Hz. The motor controller ran field-oriented control (FOC) motor commutation at 10 kHz, controlling the torque of the BLDC motor through the position feedback of the encoder (2048 counts per revolution).

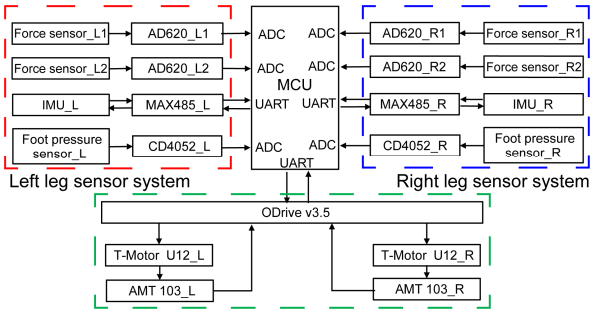

Fig. 8 Control system hardware diagram The microprogrammed control unit (MCU) collects the data of the force sensor and foot pressure sensor through ADC channels, obtains the data of the IMU through UART, and sends the command to the ODrive motor driver through UART after processing. References to color refer to the online version of this figure

2.3.2 Control strategy

The goal of the exoskeleton control strategy is to output a suitable amount of assist force based on different gait states of the subject (Jiménez-Fabián and Verlinden, 2012). The control strategy of our exoskeleton is shown in Fig. 9. The gait cycle was divided by the gait detector and different gait states corresponded to different ankle torques. We used the

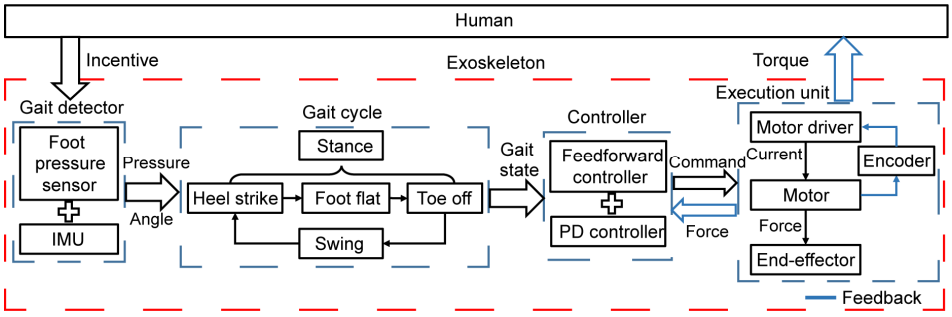

Fig. 9 Schematic of the exoskeleton architecture

The gait detector is composed of the foot pressure sensor and IMU. These can detect the human walking and identify the gait cycle. Then the controller controls the execution unit to output the desired torque to the body by the feedforward and proportional-derivative (PD) controllers according to the gait cycle

data in Novacheck (1998) as the desired torque in our prototype. The ankle torque presented in Novacheck (1998) lacked the swing phase part. However, the ankle torque does exist because the tibialis anterior muscle still acts during the swing phase (Winter, 2009). Thus, a constant assistance torque was given in the swing phase state to make our prototype provide assistance torque over the whole gait cycle. The gait cycle was divided by the gait detector presented in Section 2.3.1. The cycle of output assistance torque can be adjusted in real time according to the gait cycle change of the subject (Wu et al., 2019); i.e., the percentage of stance phase and swing occupied in one gait cycle can be predicted adaptively based on the wearer's previous step, and then the torque curve of Novacheck's research can be mapped to the new gait cycle to obtain the corresponding torque curve, i.e., to form the desired assistance torque. In other words, the desired assistance torque profile can be seen as a stretch or compression transformation along the horizontal axis of the original torque profile measured by Novacheck (1998).

To track the desired assistance torque, a controller with feedforward and feedback was designed to determine command current i_o. For feedforward control, the relationship between the motor torque and current is as follows:

$$i_{ff} = \frac{T}{k_t}, \tag{17}$$

where T is the motor output torque, k_t the torque coefficient, and i_{ff} the command current part from the feedforward control. k_t can be derived from the inherent parameter k_v as

$$k_t = \frac{60}{2\pi k_v}. \tag{18}$$

At the same time, the proportional and differential feedback closed-loop control was used as follows:

$$e(k) = T_d(k) - T_m(k), \tag{19}$$

$$i_{fb} = k_p e(k) + k_d[e(k) - e(k-1)], \tag{20}$$

where $e(k)$ is the torque error, $T_d(k)$ denotes the desired torque, $T_m(k)$ represents the measured torque, and i_{fb}, k_p, and k_d are the command current part from the feedback control, the proportional, and differential coefficients, respectively. Combining Eqs. (17) and (20), the total command current i_o can be calculated as

$$i_o = i_{ff} + i_{fb}. \tag{21}$$

Then, the BLDC motor was controlled in torque mode using FOC, a control method (Kumar and Krishnan, 2016) equivalently manipulating three-phase currents of the motor using two orthogonal DC components (i.e., direct-axis current and quadrature-axis current), as shown in Fig. 10. To achieve good dynamic torque tracking performance, two proportional-integral (PI) controllers for these two DC components were used. The measured three-phase currents of the motor are converted into the feedback values i_d, i_q. A PI controller can be achieved by the following equations:

$$\begin{cases} v_{\mathrm{d}}(t)=k_{\mathrm{dp}}[i_{\mathrm{d\_ref}}(t)-i_{\mathrm{d}}(t)]+k_{\mathrm{di}}\int[i_{\mathrm{d\_ref}}(t)-i_{\mathrm{d}}(t)]\mathrm{d}t, \\ v_{\mathrm{q}}(t)=k_{\mathrm{qp}}[i_{\mathrm{q\_ref}}(t)-i_{\mathrm{q}}(t)]+k_{\mathrm{qi}}\int[i_{\mathrm{q\_ref}}(t)-i_{\mathrm{q}}(t)]\mathrm{d}t, \end{cases} \tag{22}$$

where $v_{\mathrm{d}}(t)$ and $v_{\mathrm{q}}(t)$ are the outputs of the direct-axis PI controller and quadrature-axis PI controller at time t, respectively. $i_{\mathrm{d\_ref}}$ is the direct-axis reference current, remaining at zero (using only permanent magnet excitation), and $i_{\mathrm{q\_ref}}$ is the quadrature-axis reference current, equal to the torque command current i_{o}. k_{dp}, k_{di} are the proportional and integral constants of the direct-axis current controller, respectively, and k_{qp}, k_{qi} are the proportional and integral constants of the quadrature-axis current controller, respectively. The values of k_{qp}, k_{qi}, k_{dp}, and k_{di} depend on the inherent parameters of the motor (resistance R and inductance L) as follows:

$$\begin{cases} k_{\mathrm{dp}}=k_{\mathrm{qp}}=\text{bandwidth}\cdot L, \\ k_{\mathrm{di}}=k_{\mathrm{qi}}=\dfrac{R\cdot k_{\mathrm{dp}}}{L}. \end{cases} \tag{23}$$

In our research, the bandwidth is set as 1/20 of the current control frequency f_{cc}, i.e., bandwidth= 1/20×f_{cc}=1/20×10 kHz=500 Hz.

After the inverse Park transformation and inverse Clark transformation, the voltage vector (v_{d}, v_{q}) is transformed into three phase voltages (v_{a}, v_{b}, v_{c}) for performing pulse width modulation (PWM) to control the motor.

Then, the device will output a desired assistance torque to the human.

3 Results and discussion

The physical prototype worn on the subject is shown in Fig. 11. The whole exoskeleton weighed 7002 g, but only 2005 g (including 400 g of shoe) was placed on each leg of the subject. To verify the portability, systematic performance, and assistance effect of our exoskeleton, three experiments, i.e., gait cycle detection, biological gait torque tracking, and assistance effect evaluation by muscle activity, were implemented. The subject was a healthy person, aged 22 years, 1.80 m tall, and weighed 70 kg.

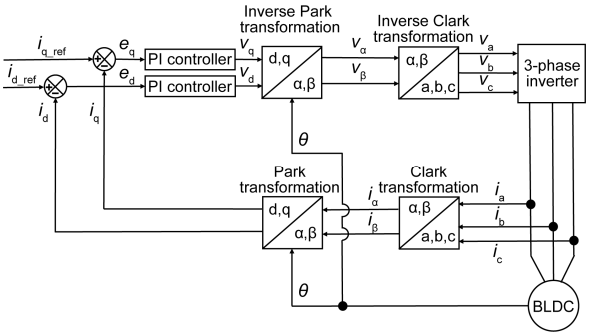

Fig. 10 Block diagram of the field-oriented control method

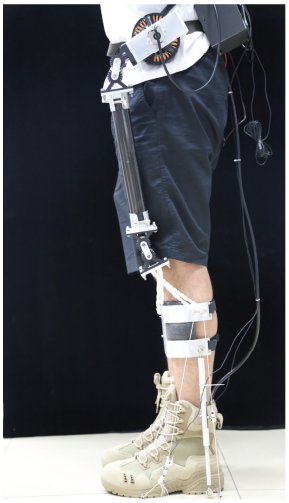

Fig. 11 An overview of the exoskeleton worn on the human body

3.1 Gait cycle detection

Three sub-experiments were conducted to test the performance of the gait cycle detection unit. Experiment I was a gait cycle detection experiment using the foot pressure sensor. Experiment II was a gait cycle detection experiment using the IMU. Finally, in experiment III, the performance of the gait detector system using both the foot pressure sensor and the IMU was validated. The subject in all three experiments walked at a speed of 3 km/h on the treadmill.

3.1.1 Experiment I: gait cycle detection using the foot pressure sensor

To detect the human gait using the foot pressure sensor as described in Table 1 (Section 2.2), the threshold of the plantar pressure on the forefoot, toe, and heel should be determined experimentally.

The pressures obtained from the subject forefoot,

toe, and heel detection units during 10 walking steps are shown in Fig. 12a. First, the minimum and maximum pressures of each unit during one step can be found. Generally, it can be concluded that the foot is off the ground (pressure state: 0) during the period of minimum pressure. The foot is on the ground (pressure state: 1) during the period of maximum pressure. Therefore, a threshold value between the maximum and minimum pressures can be found to identify the pressure unit's state. To make the threshold more robust to different situations, i.e., different walking speeds, different weights of subjects, the threshold should add 10% interval range (pressure difference between maximum and minimum) to the minimum pressure according to the experiment:

$$\text{Threshold} = \min(\text{pressure}) + [\max(\text{pressure}) - \min(\text{pressure})] \times 10\%. \quad (24)$$

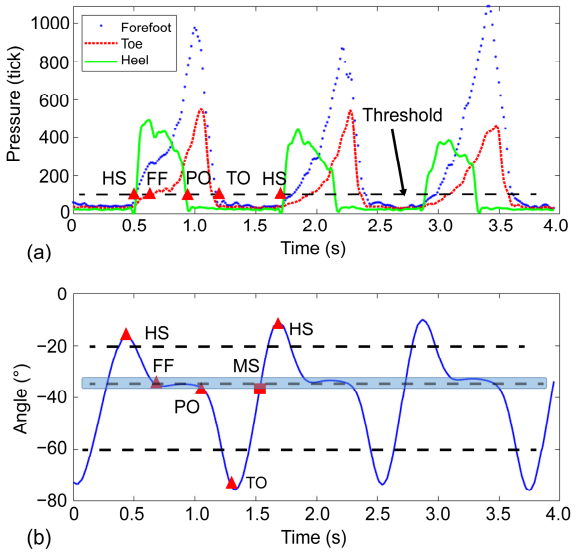

Fig. 12 Gait states identified based on data from the foot pressure sensor and the IMU

(a) represents the pressure ticks of the forefoot, toe, and heel during three cycles. The gait state, i.e., heel strike (HS), foot flat (FF), push off (PO), and toe off (TO), can be clearly distinguished by foot pressure distribution. The black dashed line is the threshold (120 ticks) of the foot pressure sensor to identify the functioning regions of the foot. (b) represents the angle φ of the IMU during three cycles. In addition to HS, FF, PO, and TO states, the mid-swing (MS) state can be clearly distinguished by angle φ. The three black dashed lines represent angle thresholds of heel strike (−20°), foot flat (−35°±2°), and toe off (−60°) to recognize the gait state, respectively. References to color refer to the online version of this figure

Nevertheless, the pressure values in different walking steps could not be kept the same. Thus, we obtained the thresholds of 10 gaits for each pressure detection unit and calculated the mean as the final threshold.

The state of each pressure detection unit can be judged by the threshold and the gait state can be identified according to Table 1.

3.1.2 Experiment II: gait cycle detection experiment using the IMU

The experiment here was using the IMU attached to the shoe to detect the gait state. The angle and angular velocity variation during one gait cycle can work well to distinguish the gait state.

The IMU data of three walking steps is shown in Fig. 12b. During the experiment, since the foot pressure sensor and the IMU were used at the same time, the gait state identified from the angle/angular velocity (collected by the IMU) and the pressure (collected by the foot pressure sensor) can be fused to obtain a better detection result. For the IMU data, three angle thresholds were chosen to identify heel strike, foot flat, and toe off. The angle threshold of foot flat floated within the range of $\pm\varepsilon_a$, where ε_a is a small value determined according to the robustness of the gait detector system. In addition, another small value ε_v of the angular velocity was needed. Moreover, the red square in Fig. 12b (same y-axis value as the foot flat) during the swing phase was defined as the mid swing, which could not be identified by the foot pressure sensor.

The method using the IMU angle and angular velocity to detect the gait cycle was developed, and the corresponding gait detection logic table according to the data of the IMU is shown in Table 2.

3.1.3 Experiment III: gait cycle detection fusion strategy

To improve gait cycle detection accuracy, a foot pressure sensor and IMU fusion strategy was conducted. The foot pressure sensor obtained the forefoot, toe, and heel pressure as shown in Fig. 13 (top), so the gait cycle can be divided according to Table 1. The IMU angle and angular velocity on the x axis are shown in Fig. 13 (middle), and the gait cycle can be divided according to Section 3.1.2. The gait cycle detection results of the two sensors were fused to

Table 2 Gait detection logic table according to the data of the IMU

Gait	Angle φ (°)	Angular velocity ω (°/s)
Heel strike	φ>Threshold (HS)	$\|\omega\|<\varepsilon_v$
Foot flat	$\|\varphi-$Threshold (FF)$\|<\varepsilon_a$	$\|\omega\|<\varepsilon_v$
Push off	$\|\varphi-$Threshold (FF)$\|>\varepsilon_a$	$\|\omega\|>\varepsilon_v$
Toe off	φ<Threshold (TO)	$\|\omega\|<\varepsilon_v$
Mid swing	$\|\varphi-$Threshold (FF)$\|<\varepsilon_a$	$\|\omega\|>\varepsilon_v$

ε_a and ε_v denote small values of the angle and angular velocity close to zero, respectively

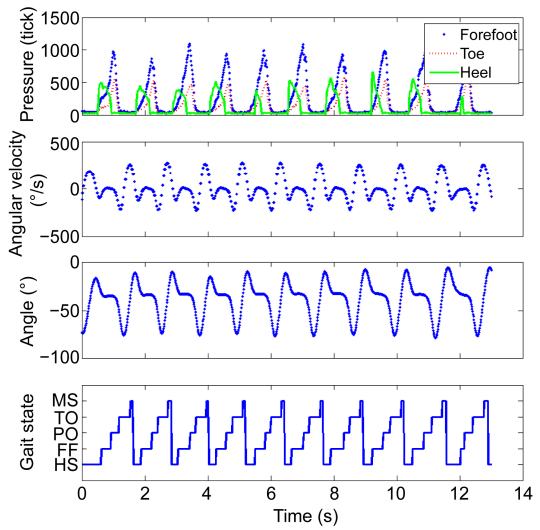

Fig. 13 Gait state detection results distinguished by foot pressure, IMU angle, and angular velocity when the subject walked at a speed of 3 km/h with the exoskeleton on
The four subplots from top to bottom are the pressure distribution measured by the foot pressure sensor, the angular velocity collected by the IMU, the pitch angle of the IMU, and the resultant gait states detected by the gait detection system, respectively

guide the control of the exoskeleton. The fusion strategy can be described as

$$t_p = k_1 t_{fps} + k_2 t_{imu}, \quad (25)$$

where t_{fps} denotes the transition time of the gait state detected by the foot pressure sensor, t_{imu} is the transition time of the gait state detected by the IMU, and k_1, k_2 are the weight parameters of the foot pressure sensor and the IMU, respectively. A multivariate linear regression method was used to determine the values of k_1 and k_2. The model can be established as

$$t_p = k_0 + k_1 t_{fps} + k_2 t_{imu} + e, \quad (26)$$

where k_0 is a constant (y-intercept at time zero) and e is the error term (residuals). A video-based experiment was designed to obtain a series of observed values of the transition time (t_p) of gait states (HS, FF, PO, TO), as shown in Fig. 14a. Using the multivariable linear regression method of MATLAB, the fusion model can be described as t_p=0.0025+0.4492t_{fps}+0.5524t_{imu} (r^2=0.999 96), as shown in Fig. 14b.

The gait cycle detected from Eq. (25) is presented in Fig. 13 (bottom). It can be concluded that the gait detection system well divided the human gait.

It is foreseeable that the angle thresholds of each gait state of the IMU will change when the subject walks on a ramp or up and down stairs, and thus we will conduct further research to improve the performance of our exoskeleton in a complex environment.

3.2 Biological gait torque tracking

To validate the power output performance of the exoskeleton, an experiment tracking the desired biological torque was implemented. During the experiment, we collected the torque output of 2-min walking steps when the subject wore the exoskeleton and walked on the treadmill at a speed of 3 km/h. As

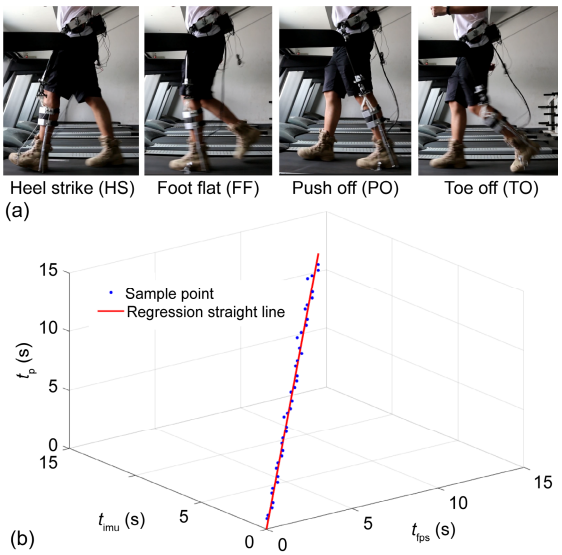

Fig. 14 Four gait transition states (HS, FF, PO, TO), determining the observed values of the transition time t_p by identifying the four transition states in the video (a) and the multivariate linear regression method used to determine k_1 and k_2 (b)
The red line in (b) is the regression result, which is used as the fusion model to predict the transition time of the gait state (t_p=0.0025+0.4492t_{fps}+0.5524t_{imu}, r^2=0.999 96). References to color refer to the online version of this figure

described in Section 2.3.2, the desired torque was a 15% biological ankle torque obtained from Novacheck (1998). The desired torque was tracked using a feedforward and feedback controller by tuning the torque coefficient k_t, proportion coefficient k_p, and differential coefficient k_d introduced in Section 2.3.2. The measured assistance torque consisted of T_h (stance phase) and T_f (swing phase), the value of which can be obtained by Eqs. (1) and (2) (Fig. 15). The x axis begins with the heel strike state (0%), and the stance and swing phases are separated by the toe off state (about 70%). In addition, the standard deviations of measured and desired torques are plotted in Fig. 15. Note that the desired torque has the standard deviations as well because the time instant of toe off state is different in each gait cycle even for the same person; that is, the duration ratios between the stance phase and the swing phase are different in each cycle.

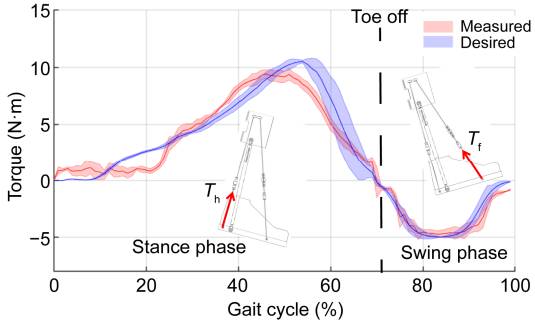

Fig. 15 Stance phase and swing phase assistance torque provided by the exoskeleton compared with the desired torque

The desired torque of the stance phase is set to 15% of the human body's normal walking biological torque. The maximum desired torque of the swing phase is set as 5 N·m. The red and blue solid lines represent the mean values of the measured and desired torques, respectively. References to color refer to the online version of this figure

When the subject walked around the foot flat state, the maximum error of the mean (2.3802 N·m) of torque tracking appeared. This happened at the beginning of the gait cycle when the device just started to work and provided a small ankle assistance torque. The system friction counterbalanced part of the output torque, which led to smaller force sensor readings. The maximum standard deviation of the desired torque was 2.5417 N·m, which means that there was a relatively large cadence difference between walking steps. The maximum standard deviation of the measured torque was 1.3557 N·m. In addition, the adaptive assistance torque for dorsiflexion provided by the bidirectional exoskeleton was conducive to rehabilitation training (Shorter et al., 2011) and played an important role in gait speed (Lin et al., 2006). These are the advantages of our prototype compared with a unidirectional device for achieving plantarflexion-dorsiflexion movement.

3.3 Assistance effect evaluation by muscle activity

A muscle activity measurement experiment was designed to preliminarily verify the short-term assistance effect of our exoskeleton on human body. The electromyography (EMG) signal of soleus (achieving plantarflexion) collected from the EMG senor (Sichiray Technology Co., Ltd., Jiangsu, China), was evaluated by the root mean square (RMS) value. During the experiment, the subject was requested to walk for 2 min (pick 1-min data in the middle for statistical analysis) at a 3 km/h speed on the treadmill with the exoskeleton on. Three experimental cases, i.e., without exoskeleton (No Exo), with exoskeleton on and power off (Power Off), and with exoskeleton on and power on (Power On), were conducted to investigate the exoskeleton assistance effect.

3.3.1 Processing of EMG signals

The measurement electrodes were attached to the soleus muscle (Fig. 16a). The EMG signal can be obtained after amplification and ADC sampling in the sensor (Fig. 16b). Then, signal processing was implemented in MATLAB R2018a; i.e., the signal was rectified and the moving average filtered. This can be expressed as

$$\mathrm{EMG_f}(i)=\frac{1}{M}\sum_{j=-(M-1)/2}^{(M-1)/2}\left|\mathrm{EMG}(i+j)\right|, \qquad (27)$$

where M is the moving window, and EMG(i) and EMG$_f$(i) are the original data and filtered data, respectively. The filtered curve is shown in Fig. 16c. Then the data was segmented by the gait cycle (Fig. 16d), and the root mean square value RMS(n) of the n^{th} gait cycle is calculated as

$$\mathrm{RMS}(n)=\frac{1}{W(n+1)-W(n)}\sqrt{\sum_{t=W(n)}^{W(n+1)}\mathrm{EMG_f^2}(t)}, \qquad (28)$$

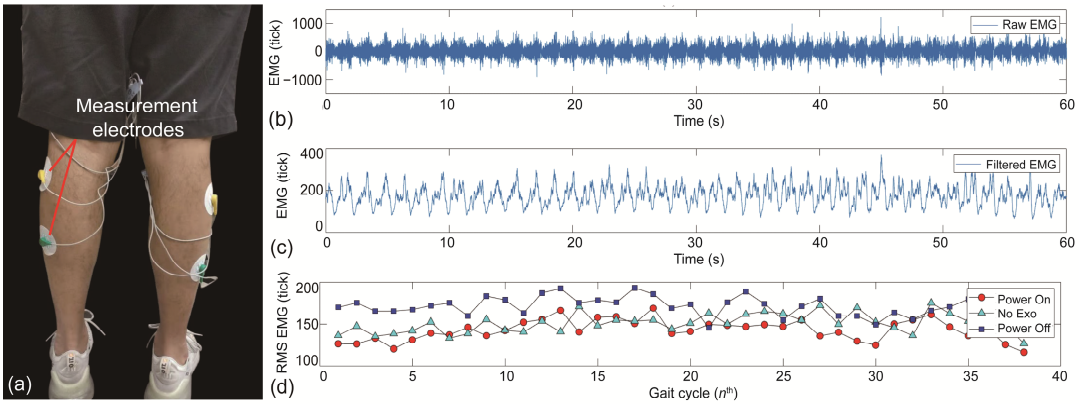

Fig. 16 Muscle activity measurement experiment: (a) measurement electrodes were attached to the soleus muscle; (b) raw EMG sampling data under the No Exo condition; (c) EMG result after being rectified and moving average filtered under the No Exo condition; (d) RMS EMG value of soleus muscle under three different conditions (No Exo, Power Off, and Power On)

where $W(n)$ is the boundary point in the n^{th} gait cycle. Therefore, the mean and standard deviation of the RMS of the EMG signal can be obtained.

3.3.2 Results and discussion

As shown in Fig. 17, the mean and standard deviation of RMS EMG are demonstrated in the form of histograms. The muscle activity of the soleus was raised by 13.9% (two-sample t test, H=1, P<0.01) when the subject wore the exoskeleton with power off because the additional mass of the exoskeleton (about 7 kg) was put on the subject. However, when the exoskeleton was at power on, the soleus's activity was reduced by 5.2% (two-sample t test, H=1, P=0.0064) compared with the without-wearing exoskeleton state, and 16.7% (two-sample t test, H=1, P<0.01) of energy was saved compared to wearing exoskeleton with power off. It can be preliminarily concluded that our exoskeleton can well assist the subject during a walking state in the short term.

Table 3 presents the comparison of assistance effect evaluation of our exoskeleton and four other previous ones (Wehner et al., 2013; Asbeck et al., 2014; Collins et al., 2015; Awad et al., 2017). It can be found that our exoskeleton is about at the same level as the four other prototypes in terms of walking enhancement under short-term assessment and training, but the advantage of our prototype is that we used one single motor to achieve ankle bidirectional assistance. This method will effectively reduce the weight and cost of the exoskeleton under the premise that appropriate assistance torque could be provided during the whole gait cycle.

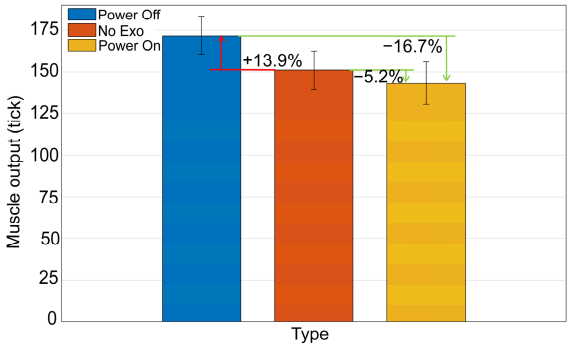

Fig. 17 Short-term effect of exoskeleton assistance on the subject soleus's activity evaluated by the RMS EMG
The soleus activity was measured under three different conditions (No Exo, Power Off, and Power On). When the subject wore the exoskeleton with power on, the soleus activity was reduced by 5.2% (two-sample t test, H=1, P=0.0064) compared to the without-wearing exoskeleton state, and 16.7% (two-sample t test, H=1, P<0.01) of energy was saved compared to wearing exoskeleton with power off

4 Conclusions

In this paper, an untethered cable-driven ankle exoskeleton using one single motor has been presented to achieve plantarflexion-dorsiflexion bidirectional ankle assistance. The end-effector was designed compatibly with user motion, and the pulley/gear-based cable transmission could promote efficiency.

Table 3 Comparison of assistance effect evaluation

Prototype	Effect evaluation					
	Weight carried	Power On versus Power Off	Power Off versus No Exo	Power On versus No Exo	Bidirection assistance	Number of actuators per leg
Soft exosuit (Wehner et al., 2013)	7.1 kg system	−10.2%	+12.8%	+1.3%	N	1
Soft exosuit (Asbeck et al., 2014)	10.1 kg system +24.5 kg payload	−6.4%	+16.7%	+9.3%	N	1
Unpowered exoskeleton (Collins et al., 2015)	0.408–0.503 kg per leg	N/A	N/A	−7.2%	N	0
Soft exosuit (Awad et al., 2017)	4.09 kg per leg	−10%±3%	N/A	N/A	Y	2
Our exoskeleton	7 kg system	−16.7%	+13.9%	−5.2%	Y	1

Also, the power output unit can self-tension the cable when the subject walks with the exoskeleton on. The gait cycle detection system based on the foot pressure sensor and the IMU was developed to identify the human gait. This provided the key features for the control strategy based on a feedforward and feedback controller for bidirectional movement assistance. Three experiments were conducted to verify the performance of the exoskeleton, including gait detector algorithm validation, biological torque tracking, and assistance effect evaluation by muscle activity. The results indicated that for the subject walking on the flat ground, the untethered cable-driven ankle exoskeleton has the following advantages: (1) The extra weight added to the wearer's legs is less and there is not much extra burden on the user; (2) The gait detection system can identify human gait states accurately and efficiently; (3) Plantarflexion-dorsiflexion bidirectional movement assistance can be provided by the exoskeleton; (4) The assistance torque provided by the exoskeleton can well track the desired ankle torque; (5) With the subject wearing the exoskeleton with the power on, the soleus muscle activity can be reduced by 5.2% compared with the without-wearing the exoskeleton state, which can potentially help the wearers reduce energy consumption.

The improvement of gait adaptability, wearing flexibility, and the enhancement of the control strategy are crucial to the performance of an exoskeleton. Also, motion assistance on different terrains, such as up-and-down-stairs and slopes, would greatly widen the application of the exoskeleton. Therefore, research will be carried out to improve the robustness and real-time performance, to develop a better torque tracking algorithm on different terrains, and to explore applications in augmentation or rehabilitation training.

Contributors

Tian-miao WANG and Xing-bang YANG conceived the project. Xuan PEI and Tao-gang HOU conducted the experiments and processed the data. Xuan YANG designed the mechanical model. Xuan PEI designed the control system and drafted the manuscript. Xing-bang YANG and Tao-gang HOU helped organize and enhance the structure and contents of the manuscript. Yu-bo FAN, Hugh M. HERR, and Xing-bang YANG helped organize the development or design of research methods. All authors provided feedback during the revision and finalization.

Acknowledgements

We appreciate Shan-yuan SONG, Qi-kai LI, and Zhen SUN from School of Mechanical Engineering and Automation of Beihang University for help in tuning the motor driver. We thank He WANG, Bu-hui JIANG, Hao-hong SU, and Si-yang ZHANG for providing comments and constructive suggestions on the controller design. We also thank Chao LIANG and Li WANG for giving some advice on data processing.

Compliance with ethics guidelines

Tian-miao WANG, Xuan PEI, Tao-gang HOU, Yu-bo FAN, Xuan YANG, Hugh M. HERR, and Xing-bang YANG declare that they have no conflict of interest.

Informed consent was obtained from all individual participants included in the experiment.

References

Asbeck AT, de Rossi SMM, Galiana I, et al., 2014. Stronger, smarter, softer: next-generation wearable robots. *IEEE Robot Autom Mag*, 21(4):22-33. https://doi.org/10.1109/mra.2014.2360283

Awad LN, Bae J, O'donnell K, et al., 2017. A soft robotic exosuit improves walking in patients after stroke. *Sci Trans Med*, 9(400):eaai9084. https://doi.org/10.1126/scitranslmed.aai9084

Bai Y, Gao XS, Zhao J, et al., 2015. A portable ankle-foot rehabilitation orthosis powered by electric motor. *Open Mech Eng J*, 9(1):982-991. https://doi.org/10.2174/1874155x01509010982

Browning RC, Modica JR, Kram R, et al., 2007. The effects of adding mass to the legs on the energetics and biomechanics of walking. *Med Sci Sports Exerc*, 39(3):515-525. https://doi.org/10.1249/mss.0b013e31802b3562

Cherry MS, Kota S, Young A, et al., 2016. Running with an elastic lower limb exoskeleton. *J Appl Biomech*, 32(3): 269-277. https://doi.org/10.1123/jab.2015-0155

Collins SH, Wiggin MB, Sawicki GS, 2015. Reducing the energy cost of human walking using an unpowered exoskeleton. *Nature*, 522(7555):212-215. https://doi.org/10.1038/nature14288

Diller S, Majidi C, Collins SH, 2016. A lightweight, low-power electroadhesive clutch and spring for exoskeleton actuation. Proc IEEE Int Conf on Robotics and Automation, p.682-689. https://doi.org/10.1109/icra.2016.7487194

Dong TY, Zhang XL, Liu T, 2018. Artificial muscles for wearable assistance and rehabilitation. *Front Inform Technol Electron Eng*, 19(11):1303-1315. https://doi.org/10.1631/FITEE.1800618

Farris RJ, Quintero HA, Goldfarb M, 2011. Preliminary evaluation of a powered lower limb orthosis to aid walking in paraplegic individuals. *IEEE Trans Neur Syst Rehabil Eng*, 19(6):652-659. https://doi.org/10.1109/tnsre.2011.2163083

Forrester LW, Roy A, Krebs HI, et al., 2011. Ankle training with a robotic device improves hemiparetic gait after a stroke. *Neurorehabil Neur Repair*, 25(4):369-377. https://doi.org/10.1177/1545968310388291

Galle S, Malcolm P, Collins SH, et al., 2017. Reducing the metabolic cost of walking with an ankle exoskeleton: interaction between actuation timing and power. *J Neuroeng Rehabil*, 14(1):35. https://doi.org/10.1186/s12984-017-0235-0

He Y, Li N, Wang C, et al., 2019. Development of a novel autonomous lower extremity exoskeleton robot for walking assistance. *Front Inform Technol Electron Eng*, 20(3):318-329. https://doi.org/10.1631/FITEE.1800561

Hou TG, Yang XB, Aiyama Y, et al., 2019. Design and experiment of a universal two-fingered hand with soft fingertips based on jamming effect. *Mech Mach Theory*, 133:706-719. https://doi.org/10.1016/j.mechmachtheory.2018.12.013

Jatsun S, Savin S, Yatsun A, 2017. Footstep planner algorithm for a lower limb exoskeleton climbing stairs. Proc 2nd Int Conf on Interactive Collaborative Robotics, p.75-82. https://doi.org/10.1007/978-3-319-66471-2_9

Jiménez-Fabián R, Verlinden O, 2012. Review of control algorithms for robotic ankle systems in lower-limb orthoses, prostheses, and exoskeletons. *Med Eng Phys*, 34(4):397-408. https://doi.org/10.1016/j.medengphy.2011.11.018

Kim S, Son Y, Choi S, et al., 2015. Design of a simple, lightweight, passive-elastic ankle exoskeleton supporting ankle joint stiffness. *Rev Sci Instrum*, 86(9):095107. https://doi.org/10.1063/1.4930561

Kuan JY, Pasch KA, Herr HM, 2018. A high-performance cable-drive module for the development of wearable devices. *IEEE/ASME Trans Mech*, 23(3):1238-1248. https://doi.org/10.1109/tmech.2018.2822764

Kumar BP, Krishnan CMC, 2016. Comparative study of different control algorithms on brushless DC motors. Proc Biennial Int Conf on Power and Energy Systems: Towards Sustainable Energy, p.1-5. https://doi.org/10.1109/pestse.2016.7516444

Kyeong S, Shin W, Yang MJ, et al., 2019. Recognition of walking environments and gait period by surface electromyography. *Front Inform Technol Electron Eng*, 20(3): 342-352. https://doi.org/10.1631/FITEE.1800601

Lairamore C, Garrison MK, Bandy W, et al., 2011. Comparison of tibialis anterior muscle electromyography, ankle angle, and velocity when individuals post stroke walk with different orthoses. *Prosthet Orthot Int*, 35(4):402-410. https://doi.org/10.1177/0309364611417040

Lin PY, Yang YR, Cheng SJ, et al., 2006. The relation between ankle impairments and gait velocity and symmetry in people with stroke. *Arch Phys Med Rehabil*, 87(4):562-568. https://doi.org/10.1016/j.apmr.2005.12.042

Mancini M, Chiari L, Holmstrom L, et al., 2016. Validity and reliability of an IMU-based method to detect APAs prior to gait initiation. *Gait Post*, 43:125-131. https://doi.org/10.1016/j.gaitpost.2015.08.015

Meijneke C, van Dijk W, van der Kooij H, 2014. Achilles: an autonomous lightweight ankle exoskeleton to provide push-off power. Proc 5th IEEE RAS/EMBS Int Conf on Biomedical Robotics and Biomechatronics, p.918-923. https://doi.org/10.1109/biorob.2014.6913898

Miller LE, Zimmermann AK, Herbert WG, 2016. Clinical effectiveness and safety of powered exoskeleton-assisted walking in patients with spinal cord injury: systematic review with meta-analysis. *Med Dev Evid Res*, 9:455-466. https://doi.org/10.2147/mder.s103102

Morris M, Shoham M, 2009. Applications and theoretical issues of cable-driven robots. Proc Florida Conf on Recent Advances in Robotics, p.1-29.

Noda T, Takai A, Teramae T, et al., 2018. Robotizing double-bar ankle-foot orthosis. Proc IEEE Int Conf on Robotics and Automation, p.2782-2787. https://doi.org/10.1109/icra.2018.8462911

Novacheck TF, 1998. The biomechanics of running. *Gait Post*, 7(1):77-95. https://doi.org/10.1016/S0966-6362(97)00038-6

Park YL, Chen BR, Pérez-Arancibia NO, et al., 2014. Design and control of a bio-inspired soft wearable robotic device

for ankle–foot rehabilitation. *Bioinspir Biomim*, 9(1): 016007. https://doi.org/10.1088/1748-3182/9/1/016007

Ruiz AF, Forner-Cordero A, Rocon E, et al., 2006. Exoskeletons for rehabilitation and motor control. Proc 1st IEEE/RAS-EMBS Int Conf on Biomedical Robotics and Biomechatronics, p.601-606. https://doi.org/10.1109/biorob.2006.1639155

Rupal BS, Singla A, Virk GS, 2016. Lower limb exoskeletons: a brief review. Proc 22nd National Conf on Mechanical Engineering and Technology, p.130-140.

Sankai Y, 2010. HAL: hybrid assistive limb based on cybernics. In: Kaneko M, Nakamura Y (Eds.), Robotics Research. Springer Berlin Heidelberg, p.25-34. https://doi.org/10.1007/978-3-642-14743-2_3

Sawicki GS, Khan NS, 2016. A simple model to estimate plantarflexor muscle–tendon mechanics and energetics during walking with elastic ankle exoskeletons. *IEEE Trans Biomed Eng*, 63(5):914-923. https://doi.org/10.1109/tbme.2015.2491224

Shorter KA, Kogler GF, Loth E, et al., 2011. A portable powered ankle-foot orthosis for rehabilitation. *J Rehabil Res Dev*, 48(4):459-472. https://doi.org/10.1682/jrrd.2010.04.0054

Stewart JD, 2008. Foot drop: where, why and what to do? *Pract Neurol*, 8(3):158-169. https://doi.org/10.1136/jnnp.2008.149393

Taborri J, Palermo E, Rossi S, et al., 2016. Gait partitioning methods: a systematic review. *Sensors*, 16(1):66. https://doi.org/10.3390/s16010066

Wehner M, Quinlivan B, Aubin PM, et al., 2013. A lightweight soft exosuit for gait assistance. Proc IEEE Int Conf on Robotics and Automation, p.3362-3369. https://doi.org/10.1109/icra.2013.6631046

Winter DA, 2009. Biomechanics and Motor Control of Human Movement. Wiley, Hoboken, USA.

Witte KA, Zhang JJ, Jackson RW, et al., 2015. Design of two lightweight, high-bandwidth torque-controlled ankle exoskeletons. IEEE Int Conf on Robotics and Automation, p.1223-1228. https://doi.org/10.1109/icra.2015.7139347

Wu A, Yang XB, Kuan JY, et al., 2019. An autonomous exoskeleton for ankle plantarflexion assistance. Int Conf on Robotics and Automation, p.1713-1719. https://doi.org/10.1109/icra.2019.8793913

Zhang YF, Kleinmann RJ, Nolan KJ, et al., 2019. Preliminary validation of a cable-driven powered ankle–foot orthosis with dual actuation mode. *IEEE Trans Med Robot Bion*, 1(1):30-37. https://doi.org/10.1109/tmrb.2019.2895787

Zoss A, Kazerooni H, Chu A, 2005. On the mechanical design of the Berkeley Lower Extremity Exoskeleton (BLEEX). IEEE/RSJ Int Conf on Intelligent Robots and Systems, p.3465-3472. https://doi.org/10.1109/iros.2005.1545453